DE GRUYTER High Temperature Materials and Processes 2023; 42: 20220253

Research Article

Shaogang Wang*, Junke Xu, and Yongpeng Wang

Effect of post-weld heat treatment on 6156 aluminum alloy joint formed by electron beam welding

https://doi.org/10.1515/htmp-2022-0253
received August 23, 2022; accepted November 02, 2022

Abstract: The 6156 aluminum alloy is welded by electron beam welding, and different post-weld heat treatments (PWHTs) are carried out on the joints. The microstructure, mechanical property, and corrosion behavior of the welded joint before and after PWHT are investigated, respectively. Results show that the fusion zone is composed of columnar crystal and equiaxed grain in as-welded (AW) condition. There are mainly α-Al matrix phase, and some strengthening phases β″(Mg_2Si) and Q ($Al_4CuMg_5Si_4$) in weld metal. After PWHT, the quantity of strengthening phases in weldment is greatly increased, and their distribution is also improved. The tensile strength of welded joint is 65.8% of that of the base metal (BM) in AW condition. After the heat treatment of HT2, the strength coefficient of joint reaches 85.1%. There are many dimples on the tensile fracture surface, and the joint obviously presents the characteristic of ductile fracture. The electrochemical corrosion performance and resistance to intergranular corrosion of weldment in AW condition are higher than that of the BM. However, they are decreased to a certain extent after PWHT. Compared with that of the AW joint, the resistance to intergranular corrosion is slightly decreased after PWHT, and that of the HT2 joint is the best among them.

Keywords: 6156 aluminum alloy, electron beam welding, post-weld heat treatment, microstructure and property, corrosive behavior

1 Introduction

The 6××× series (Al–Mg–Si) aluminum alloys have higher specific strength and good corrosion resistance, and they are widely used in many industrial fields such as aerospace, rail transportation, chemical machinery, etc. [1]. For example, the 6056 and 6156 aluminum alloys were used to fabricate the structural parts of aircraft, which could obviously reduce their weights [2]. In industrial production, aluminum alloys are often used as welded structure. The main welding methods for aluminum alloys involve friction stir welding [3,4], laser beam welding [5], and metal inert gas (MIG) welding [1]. However, during the fusion welding of aluminum alloys, welding defects such as weld porosity, grain coarsening, and hot cracking were probably generated [6]. Compared with the conventional welding process, electron beam welding (EBW) has the feature of high energy density and deep penetration ability, which are beneficial to obtain welded joint with large depth to width ratio. Moreover, EBW is usually conducted in vacuum environment, and welding defects such as weld porosity can be significantly reduced. Consequently, the welded joint with good quality is easily obtained.

The 6××× series aluminum alloys belong to the heat-treatable strengthening alloys. During the welding process, the microstructure of welded joint will be changed under the effect of weld thermal cycle, which leads to the softening phenomenon in weld zone [3,4]. The appropriate post-weld heat treatment (PWHT) is often required, so that the mechanical property of welded joint could be improved [7]. Wang et al. [8] conducted the laser–tungsten inert gas hybrid welding of 6061-T6 alloy. By the optimization of welding procedure, and solution and aging treatment on the joint after welding, the grains in weldment were refined, and the distribution of precipitates was improved [3,8]. As a result, the mechanical property of joint was increased. Viscusi et al. [9] studied the AA6156/AA2139 and AA6156/PA765 dissimilar alloys

---

*** Corresponding author: Shaogang Wang,** College of Materials Science and Technology, Nanjing University of Aeronautics and Astronautics, Nanjing, 211106, China, e-mail: sgwang@nuaa.edu.cn
Junke Xu, Yongpeng Wang: College of Materials Science and Technology, Nanjing University of Aeronautics and Astronautics, Nanjing, 211106, China

T-joints by double-beam laser welding with filler wire, and the effect of PWHT was discussed. Results showed that heat treatment had great effect on the content and distribution of Cu and Zn elements in weldment, which led to obvious difference in the mechanical property of the two joints.

The 6××× series aluminum alloys had good corrosion resistance [6,10]. However, the content of alloying elements in aluminum alloy as well as the heat treatment process had great influence on its corrosion resistance [11–13]. In addition, during the fusion welding process, the chemical composition and microstructure of weld metal are greatly changed compared with that of the base metal (BM). Under different welding parameters and PWHT processes, the corrosion resistance to weld zone is different. Kermanidis et al. [14] studied the corrosion fatigue behavior of 6156-T3 alloy laser welded joint after PWHT T8. The corrosion susceptibility to weldment was increased to a certain extent. After salt spray corrosion, the fatigue performance of the welded joint was decreased, and the corrosion pit became the initial position of fatigue crack.

Zhou et al. [15] studied the effect of laser power on microstructure and corrosion resistance of 6061 alloy joints. The pitting corrosion was mainly due to the existence of Mg_2Si phase or intermetallic compound particles (Al-Fe-Si) in the weldment. Sun et al. [16] investigated the electrochemical corrosion behavior of 6005A alloy and its joint, and the mechanism of corrosion fatigue crack was explored. The more the inclusions and welding defects in the weldment, the lower the corrosion resistance was to the weldment. Sravanthi et al. [17] analyzed the effect of welding parameters on the corrosion resistance of 6061 aluminum alloy/galvanized mild steel dissimilar EBW joint. The intergranular corrosion in the weldment was due to the formation of micro-galvanic couple by the Al–Fe–O particles and the Al–Mg–Si precipitates. Intergranular corrosion usually occurred at the interface between the weldment and the BM.

At present, investigation on the effect of PWHT on the microstructure and mechanical property of 6156 alloy EBW joint is still insufficient, and the relationship between the microstructure and the mechanical property need to be well understood. In addition, there are few reports on the corrosion behavior of 6156 alloy EBW joint. In the present work, the 6156 alloy is welded by using EBW. The microstructure, mechanical property, and corrosion behavior of 6156 alloy EBW joint before and after PWHT are investigated. As a result, some technical guidance and practical evidence can be provided for the fabrication of welded structure.

2 Experimental material and procedure

2.1 BM and welding parameters

The BM is 6156 aluminum alloy plate with a thickness of 4 mm, and its heat treatment condition is T4 (solution treatment and natural aging). The chemical composition and mechanical property of BM are given in Table 1. The BM is machined to a welding sample with the dimensions of 150 mm × 50 mm × 4 mm by using wire electrical discharge machining (WEDM). Before welding, the welding sample is cleaned by mechanical and chemical cleaning, and the oxide film and contaminants on the sample surface are thoroughly removed.

The joint type is butt joint, and the samples are welded by using 15E500 type vacuum EBW machine. The schematic diagram of the welding process is shown in Figure 1. In order to select the suitable welding parameters, some attempt welding is carried out. Based on the observation of weld morphology, combined with the tests of joint mechanical property, the welding procedure is optimized. In the present work, the welding parameters

Table 1: Chemical composition and mechanical property of BM

Element content (wt%)	**Mg** **0.9**	**Si** **1.0**	**Cu** **0.9**	**Mn** **0.6**	**Al** **Bal.**
Tensile strength (MPa)			322.0		
Elongation (%)			18.2		

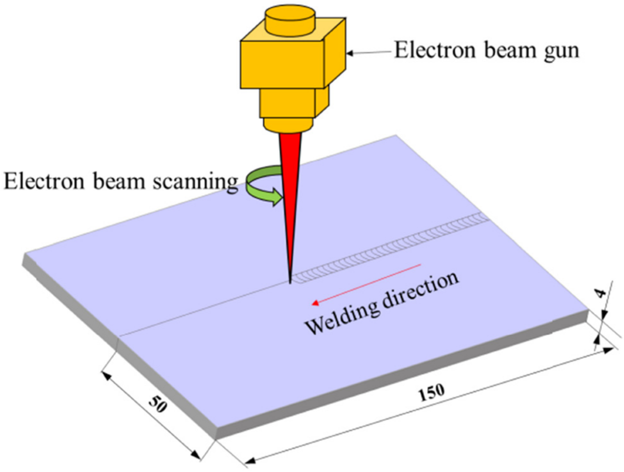

Figure 1: Schematic diagram of EBW process.

are determined as follows: the pressure of vacuum chamber is 8×10^{-3} Pa, acceleration voltage is 60 kV, electron beam current is 25 mA, focusing current is 570 mA, welding speed is 16 mm·s^{-1}, and working distance is 420 mm. Moreover, in order to improve the appearance of weld and reduce the weld porosity, the circular electron beam scanning is used during welding, and the scanning frequency is 500 Hz and scanning amplitude is 1%. Several samples are welded by the above welding procedure, and the welded joints with good morphology are obtained. No welding defects such as micro-crack and gas pores are generated.

2.2 PWHT

Due to the softening phenomenon of weld zone in as-welded (AW) condition, in order to improve the microstructure of weld zone and promote the precipitation of strengthening phase in weldment, the NBD-M1200-10IC type resistance furnace is used for the PWHT of joint. In terms of the chemical composition of BM, the scheme of post-weld solution and aging treatment to joints is listed in Table 2.

Table 2: PWHT procedure of joint

Sample no.	Solution treatment	Aging treatment
HT1	550°C × 60 min	175°C × 5 h
HT2		175°C × 15 h
HT3		175°C × 25 h

2.3 Microstructure analysis and mechanical property test

For the welded joint before and after heat treatment, microstructure analysis and property test samples are extracted by using WEDM, as shown in Figure 2. The weld zone of metallographic sample is etched by the Keller reagent (volume fraction: 2.5% HNO_3 + 1.5% HCl + 1.0% HF + 95% H_2O). Leica DMILM optical microscope and Quanta 200 scanning electron microscope (SEM) are used to observe the microstructure of joint, and the energy dispersive spectrometer (EDS) is used to identify the chemical composition of local region in weldment. D8 Advance X-ray diffractometer (XRD) is used to determine the phase constituent of weld metal. JEM-2000F transmission electron microscope (TEM) is used to analyze the substructure of fusion zone (FZ). Tensile tests of joints at room temperature are carried out by using CMT-5105 electronic universal testing machine, and the loading rate is 1 mm·min^{-1}. The tensile fracture morphology of joint is observed by using SEM. The microhardness in weld zone is measured by using HXS-1000A hardness tester, with a load of 200 g and duration time of 15 s.

2.4 Evaluation of corrosion resistance

Zahner type electrochemical workstation with three-electrode system is used to measure the potentiodynamic polarization curves (Tafel curves) of joints before and after heat treatment, and that of the BM is also conducted for comparison. In the electrochemical corrosion process,

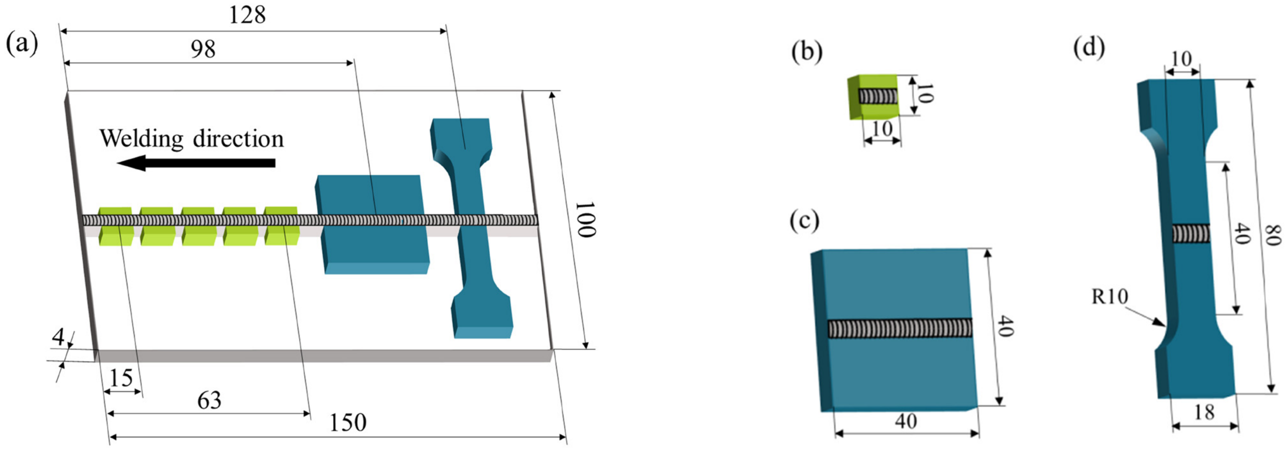

Figure 2: Schematic diagram of extracting position and dimensions for analysis samples: (a) extracting position of sample, (b) microstructure analysis sample, (c) corrosion sample, and (d) tensile sample.

the reference electrode is saturated calomel electrode, and the auxiliary electrode is platinum electrode. The BM, AW joint, and PWHT joint are prepared for the working electrode, respectively, and the working area of sample is 0.4 cm^2. The corrosive medium is 3.5% NaCl aqueous solution. The sample is immersed in corrosive solution for 10 min, and the Tafel curve is tested after the open circuit potential is stable.

According to the standard of ASTM G110-92 (2015), intergranular corrosion test of the joint is conducted. The composition of corrosion solution is as follows (volume 1 L): 57 g NaCl + 10 mL of 30% H_2O_2 + water (Bal.). The ratio of solution volume to sample area is 20 $mL \cdot cm^{-2}$. During the intergranular corrosion process, the solution temperature is constant at 30 ± 3°C. The sample is immersed in the solution for 24 h. Subsequently, the corrosion morphology of sample is observed, and the depth of intergranular corrosion is recorded.

3 Results and discussion

3.1 Microstructure of welded joint

3.1.1 Metallographic observation and phase constituent analysis

The cross section morphology and microstructure of the welded joint under different conditions are shown in Figure 3. In AW condition, the microstructure of BM presents the stripe distribution, as shown in Figure 3(b). The FZ consists of columnar crystal and equiaxed grain. The weldment near the heat-affected zone (HAZ) is columnar crystal which grows perpendicular to the fusion line, and the weld center is fine equiaxed grain. During EBW process, the temperature in weld center is the maximum, and it gradually decreases from the weld center to BM. At a distance away from the weld center, the temperature is decreased obviously, and the temperature gradient in weld center is lower. During the solidification process of molten pool, the growth rate of grains is different. Grains whose growth direction is same as the temperature gradient (perpendicular to the fusion line) will grow rapidly, while that of others is relatively slow. Consequently, the columnar crystal is formed near the fusion line.

As shown in Figure 3(c), the weld center is fine equiaxed grain, and its grain size is smaller than that of the HAZ near fusion line. It is because the temperature gradient is decreased with the growth of columnar crystal. In the growth front of columnar crystal, solute atoms are enriched at the interface of solid/liquid phase, which results in constitutional supercooling. According to the theory of liquid metal solidification, constitutional supercooling would occur in terms of the equation (1) [18].

$$\frac{G}{R} < \frac{m_L C_0 (1 - k_0)}{D_L k_0}, \tag{1}$$

where G is the temperature gradient of interfacial liquid phase, R is the growth rate of crystal, m_L is the slope of liquidus in phase diagram, C_0 is the solute concentration of interfacial solid phase, D_L is the diffusion coefficient of solute, and K_0 is the equilibrium partition coefficient of solute. When the constitutional supercooling meets the required supercooling degree for nucleation, a large number of nuclei are generated in the weld center, thus the fine equiaxed grain is formed. After PWHT, the grain size in FZ is changed, as shown in Figure 3(f), (i), and (l). The average grain size is calculated by the formula (2) given as:

$$L_M = N\lambda, \tag{2}$$

where L_M is the length of the measurement line, N is the number of grains along the measurement line, and λ is the average grain size. In AW joint, the λ value is 10.94 μm. After PWHT, the λ value in HT1 condition is 13.46 μm, HT2 condition is 14.58 μm and HT3 condition is 17.50 μm. It can be concluded that after PWHT, the grain size in weld center is increased to a certain extent.

In order to identify the phase constituent of weldment, X-ray diffraction analyses are conducted on the weld metal before and after PWHT, and the results are shown in Figure 4. There are mainly α-Al matrix phase, and $\beta''(Mg_2Si)$ and $Q(Al_4CuMg_5Si_4)$ strengthening phases in the weldment. Compared with that of the AW joint, the quantity of β'' phase and Q phase in the weldment is obviously increased after HT2 heat treatment. It demonstrates that proper PWHT can promote the precipitation of strengthening phase in the weldment, which is advantageous to the mechanical property of welded joint.

3.1.2 Precipitates and EDS analyses

In order to understand the distribution of precipitated phases, SEM observation and analysis are carried out on the weld zone. Figure 5 shows the SEM images and EDS analysis results of FZ before and after PWHT. There are obvious differences in the size and distribution of precipitates under different conditions. According to the chemical composition of BM and the results of XRD

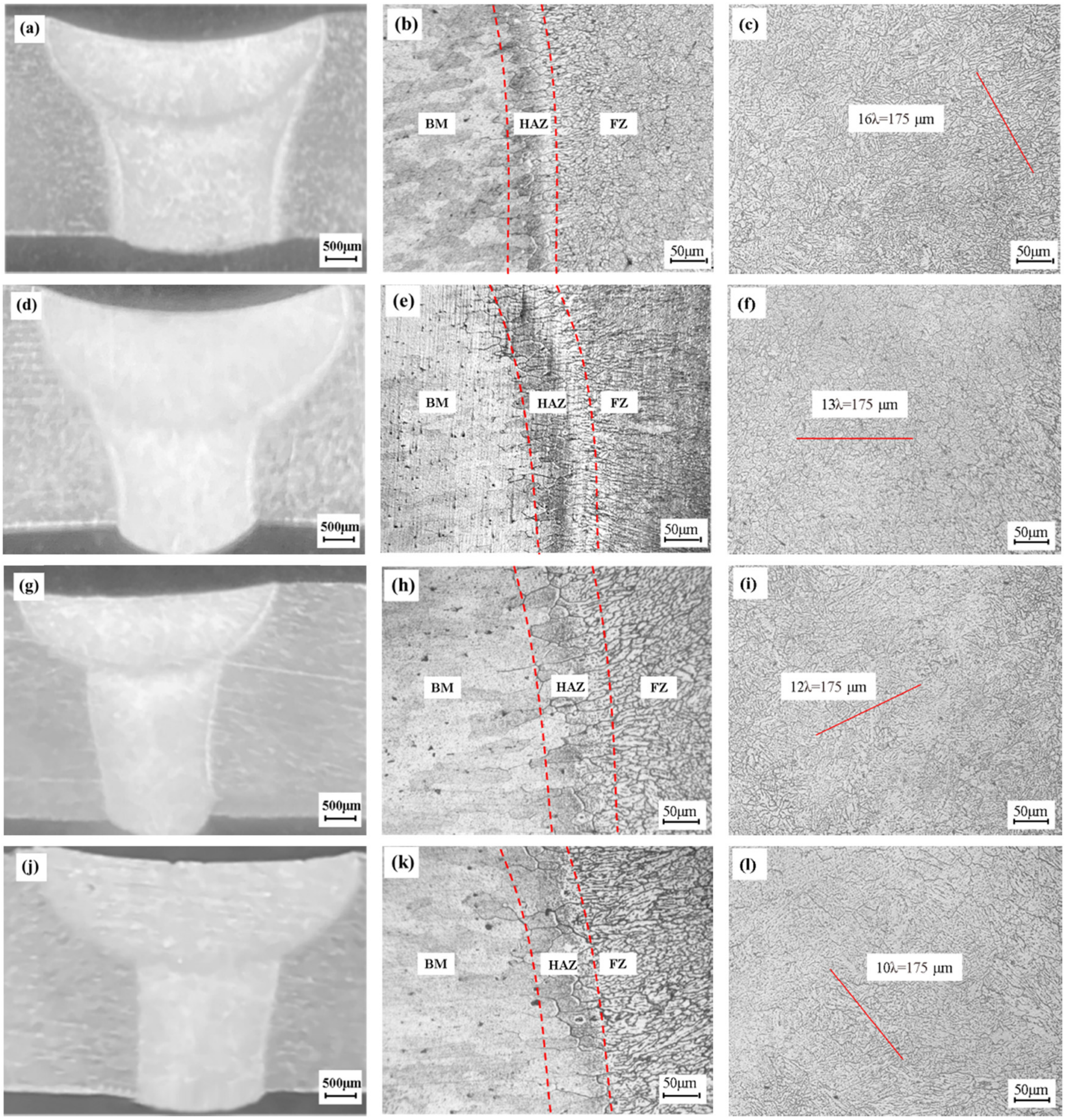

Figure 3: Cross section morphology and microstructure of welded joint under different conditions: (a–c) AW joint, (d–f) HT1 joint, (g–i) HT2 joint, and (j–l) HT3 joint.

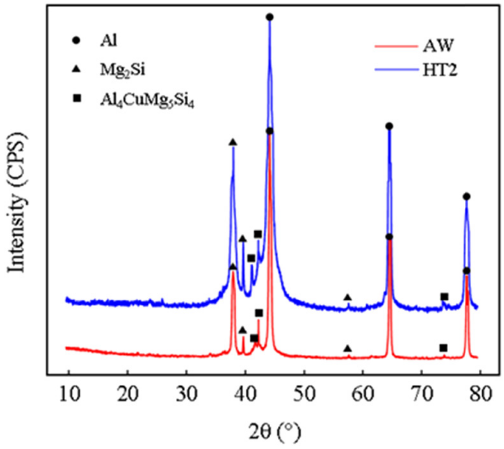

Figure 4: XRD patterns of weldment before and after PWHT.

analysis, the main precipitated phase is β″(needle-like, point-like Mg_2Si phase) in AW joint. After PWHT, the quantity of precipitates is obviously increased in the weldment, and its morphology is also varied. In the HT1 and HT3 joints, the size of precipitates is increased, and they are mainly distribute at the grain boundaries, as shown in Figure 5(c) and (g). The size of precipitates is slightly increased in the HT2 joint, and their distribution is relatively uniform, as shown in Figure 5(e). Compared with those of HT1 and HT3 joints, the distribution of precipitates at grain boundaries is reduced to a certain extent in the HT2 joint.

The EDS analysis of point A is shown in Figure 5(b). The element Mg/Si ratio to precipitated phase is 0.03 in the AW joint, which is lower than 1.73 in the Mg_2Si phase.

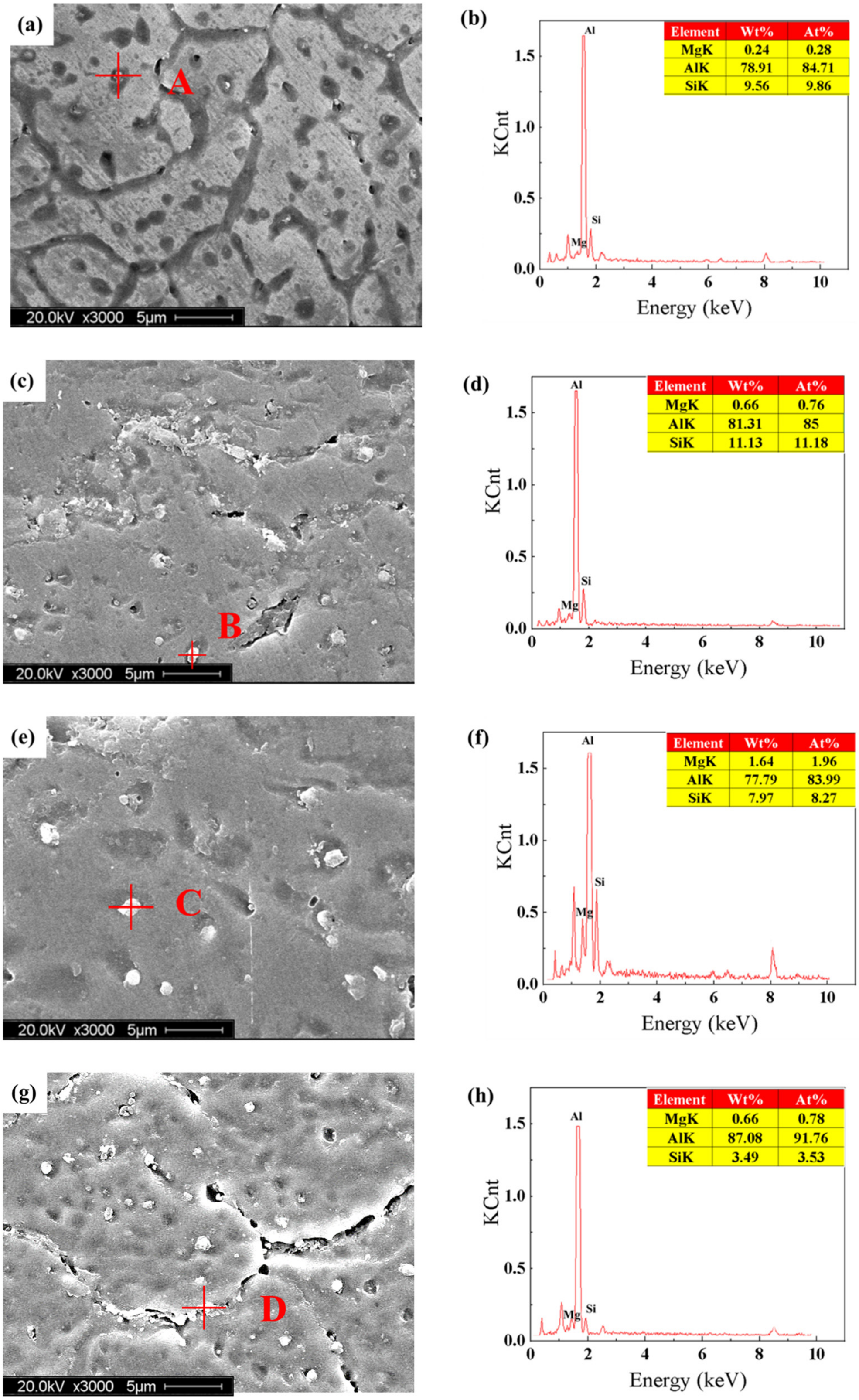

(b)

Element	Wt%	At%
MgK	0.24	0.28
AlK	78.91	84.71
SiK	9.56	9.86

(d)

Element	Wt%	At%
MgK	0.66	0.76
AlK	81.31	85
SiK	11.13	11.18

(f)

Element	Wt%	At%
MgK	1.64	1.96
AlK	77.79	83.99
SiK	7.97	8.27

(h)

Element	Wt%	At%
MgK	0.66	0.78
AlK	87.08	91.76
SiK	3.49	3.53

Figure 5: SEM images and EDS analyses of FZ under different conditions: (a) SEM image of FZ in AW joint, (b) EDS analysis of point A, (c) SEM image of FZ in HT1 joint, (d) EDS analysis of point B, (e) SEM image of FZ in HT2 joint, (f) EDS analysis of point C, (g) SEM image of FZ in HT3 joint, and (h) EDS analysis of point D.

Mg element is one of the main alloying elements in 6156 alloy, and its boiling point is relatively low, thus Mg element is probable evaporation loss during EBW process. Except for the precipitated phases containing Mg and Si elements, in the 6156-T4 alloy, there also exist some aggregation regions of Si atoms in the Al matrix, namely Guinier-Preston (GP) zone. They are some spherical flocculent groups without independent lattice structure, which can improve the mechanical performance of 6156 alloy. On the whole, the quantity of precipitates is relatively low in the AW joint.

The EDS analyses of points B, C, and D are shown in Figure 5(d), (f), and (h), respectively. The content of Mg element in precipitated phase is increased after PWHT. It is speculated that PWHT can promote the precipitation of Mg-containing phase. The element Mg/Si ratios to precipitated phases in HT1, HT2, and HT3 joints are 0.06, 0.21, and 0.19, respectively. After PWHT, the element Mg/Si ratio is increased to a certain extent, and the relative content of Si element is decreased. It means that the GP zone with the aggregation of Si atoms is transformed into the precipitated phase $\beta''(Mg_2Si)$ after PWHT, thus the quantity of β'' phase precipitated in the weldment is increased. The β'' phase has the coherent or semi-coherent relationship with the Al matrix, which results in the strengthening effect to weldment.

3.1.3 TEM analysis of weldment

The weldments of AW joint and HT2 joint are observed, respectively, and their TEM images are shown in Figure 6. From Figure 6(a), it can be seen that a large number of GP zones formed by atomic flocculent groups are distributed in the AW joint. As shown in Figure 6(b), the precipitation of strengthening phase within grains is less, and there exists a small amount of precipitated phase. Under the action of external stress, the resistance to the movement of dislocations is lower. It means that the strength and hardness of the welded joint are decreased compared to that of the BM. Investigation showed that the GP zone formed in the artificially aged 6××× aluminum alloy was more stable than that of the natural aging condition [19]. The GP zone easily became the nucleus for the precipitation of β'' phase. The content and distribution of Si element in the weldment can be improved after appropriate PWHT, and the transformation from GP zone to β'' phase is promoted; thus the mechanical property of joint is increased.

Figure 6(c) and (d) show the TEM images of weldment in HT2 condition. The distribution of precipitates in the weldment is relatively uniform, and the quantity of β'' phase is significantly larger than that of the AW joint. In addition, dislocations with high density appear in the weldment [6], as shown in Figure 6(e). The quantity of strengthening phases is increased in the weldment, and the resistance to the movement of dislocations is enhanced. The interaction among atoms at the α-Al matrix/second phase interface and the dislocations pile-up led to hindering effect of the interface on the dislocation movement, which was favorable for the tensile strength of aluminum alloys [20]. According to the Orowan mechanism, the dislocations move with the mode of bypassing the precipitated phase, and the stress field is generated. As a result, the plastic deformation of material is difficult under the action of external stress, and the mechanical property of joint is improved.

3.2 Mechanical property of joint

3.2.1 Tensile property and fracture analysis

The results of tensile tests under different conditions are listed in Table 3, and the corresponding tensile stress–strain curves of the joints are shown in Figure 7. It can be seen that the joint presents continuously plastic deformation during stretching, and no obvious yield platform occurs. Compared with that of the BM, the tensile strength of welded joint is decreased to a certain extent. The tensile strength of AW joint is 212 MPa, which is 65.8% of that of the BM. During the EBW of 6156 alloy, under the action of electron beam heat source, strengthening phases in the original BM are dissolved in the α-Al matrix. Due to the rapid cooling rate of molten pool, the quantity of precipitated phases in the weldment is less in AW condition, which results in the decrease in the joint mechanical property.

The tensile strength of joint is obviously increased after PWHT, and its elongation is also improved to a certain extent. The tensile strength of HT2 joint is 273.9 MPa, which is 85.1% of that of the BM. The tensile strength of HT2 joint is 29.2% higher than that of the AW joint. From the microstructure analyses in Figures 4 and 5(e), the quantity of precipitated phases is relatively large in the weldment of HT2 joint. Consequently, the mechanical property of HT2 joint is significantly improved, and it has the maximum tensile strength among the three PWHT joints. In the present work, the suitable PWHT procedure is HT2, namely, solution treatment at 550°C × 60 min and then artificial aging at 175°C × 15 h.

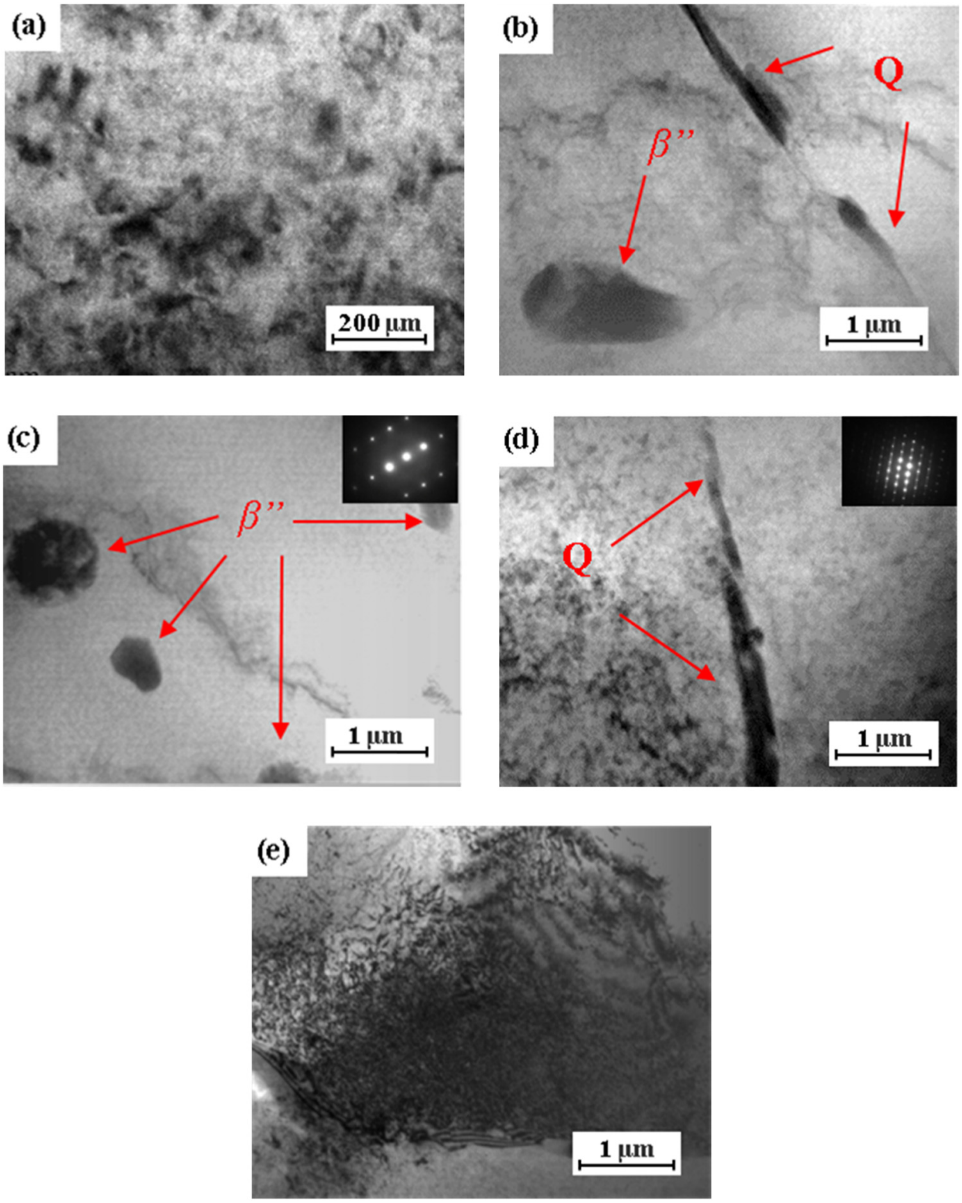

Figure 6: TEM images of the weldment: (a) atomic clusters in AW joint, (b) precipitates within grains in AW joint, (c) precipitated phase β″ in the weldment of HT2 joint, (d) precipitated phase *Q* in the weldment of HT2 joint, and (e) dislocations in the weldment of HT2 joint.

Table 3: Tensile test results of joints under different conditions

Sample no.	AW	HT1	HT2	HT3
Tensile strength (MPa)	212.0	228.7	273.9	262.1
Joint coefficient (%)	65.8	71.0	85.1	81.4
Elongation (%)	2.5	5.2	5.6	4.6

Usually, the tensile fracture mode of joint mainly depends on its microstructure. Under different conditions, the tensile fracture morphologies of joints are different, and their SEM images are shown in Figure 8. From Figure 8(a), it can be seen that there are a large number of dimples on the fracture surface of AW joint, but the size and depth of dimple are smaller. It mainly presents the characteristic of ductile fracture. During the stretching process, micropores initiate at the inclusions and second phase particles. With the continuous stretching process, local necking down appears, and the micropores aggregate to form microcracks. Crack propagation leads to the joint fracture finally.

Scanning image of the tensile fracture of HT1 joint is shown in Figure 8(b). There are some tear ridges and steps on the fracture surface, and many dimples are

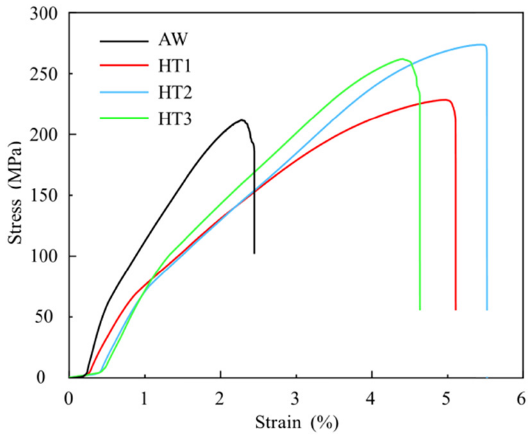

Figure 7: Tensile stress–strain curves of joints under different conditions.

distributed on the fracture surface. The tensile fracture presents the mode of quasi-cleavage fracture, which is characterized by the ductile–brittle hybrid fracture. As shown in Figure 8(c), there are tear ridges on the fracture surface of HT2 joint. Moreover, a large number of dimples are uniformly distributed on the fracture surface, and the characteristic of ductile fracture is obvious. Scanning image of the tensile fracture of HT3 joint is shown in Figure 8(d). Its fracture morphology is similar to that of the HT1 joint. There are many tear ridges, steps, and dimples on the fracture surface. The tensile fracture mode of the joint is quasi-cleavage fracture.

There are both "brittle zone" and "plastic zone" in the tensile fracture of HT1 and HT3 joints. During the tensile process, crack initiation involves the processes of cleavage and deformation cracking. The fracture mode of both the joints is quasi-cleavage fracture. In comparison, the fracture surface of HT2 joint is mainly composed of a large number of dimples distributed uniformly. It demonstrates that proper PWHT can promote the precipitation of strengthening phase in the weldment. The strength and hardness of joint are increased, and its plasticity is also improved, which is consistent with the tensile test results of the welded joint.

3.2.2 Microhardness distribution in weld zone

The microhardness distribution curves of joints under different conditions are shown in Figure 9. In AW condition, the average hardness in FZ is 76.3 HV, and in BM is 109.9 HV. Compared to that of the BM, the hardness in weld zone is obviously decreased, which is related to the

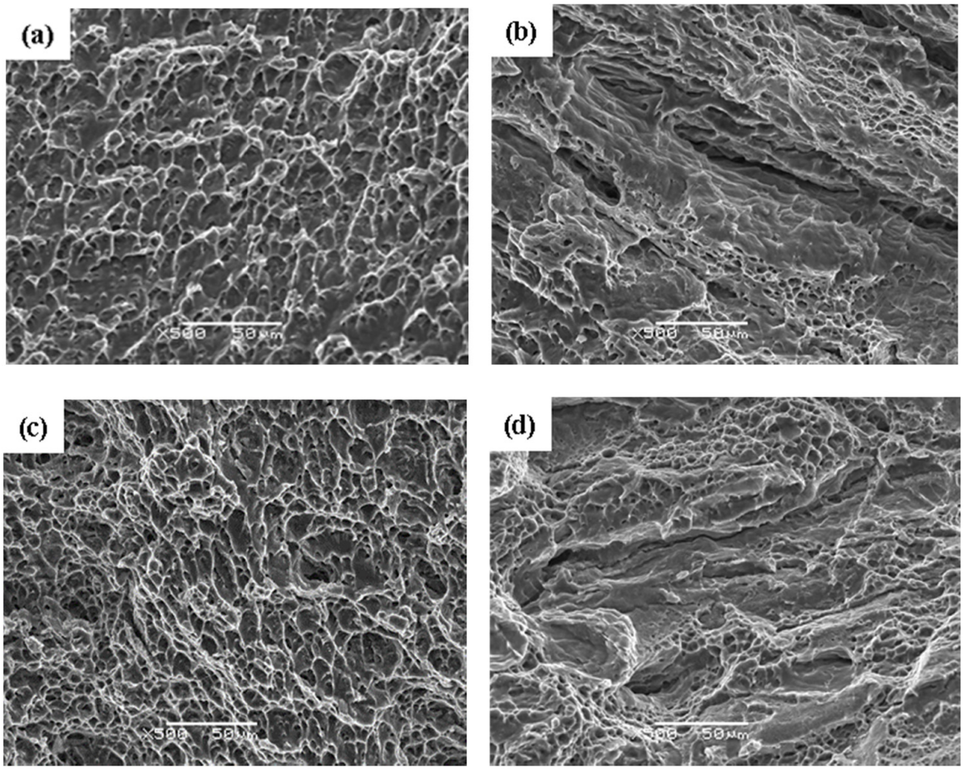

Figure 8: Scanning images of tensile fractures of joints under different conditions: (a) AW joint, (b) HT1 joint, (c) HT2 joint, and (d) HT3 joint.

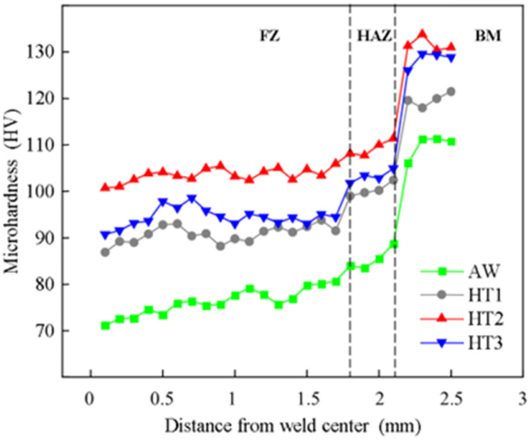

Figure 9: Microhardness distribution curves of joints under different conditions.

less strengthening phases in weld zone of the AW joint. During the EBW process, the microstructure in HAZ is changed due to the effect of weld thermal cycle, and the quantity of strengthening phases in HAZ is generally larger than that in the weldment. Consequently, the hardness in HAZ is higher than that of the FZ. Compared to that of the BM, the hardness in HAZ is still decreased to a certain extent.

The average hardness in FZ of HT2 joint is 103.5 HV. The hardness in FZ is 35.6% higher than that of the AW joint. The main strengthening phase is Mg_2Si phase in the 6××× series aluminum alloys. On the one hand, during EBW process, the strengthening phases in original BM are dissolved in the Al matrix. On the other hand, the cooling rate of molten pool is rapid, thus the quantity of precipitates in the weldment is less in AW condition. By post-weld solution treatment to the joint, elements Mg and Si were dissolved in the Al matrix to form supersaturated solid solution [21]. At the initial stage of aging, the β″ phase is precipitated, and it has the coherent or semi-coherent relationship with the Al matrix. With the prolongation of aging time, the quantity of β″ phase in the weldment is increased. A large amount of β″ phase can inhibit the movement of dislocations, which leads to the increase in the strength and hardness of the joint. However, if the aging time is too long, the quantity of precipitates in the weldment will not further increase, and the over-aging will be generated. At this time, the β″ phase would transform into equilibrium β phase (rod-like Mg_2Si phase) [22], which no longer had the coherent relationship with the Al matrix, thus the strength and hardness of the joint were slightly decreased. In summary, proper PWHT on joint can make the second phases reprecipitate in the Al matrix, which results in the great increase in hardness in FZ.

3.3 Evaluation of joint corrosion resistance

3.3.1 Electrochemical corrosion behavior

The electrochemical corrosion parameters of the BM and joints before and after PWHT in 3.5% NaCl solution are shown in Table 4. The Tafel curves of the AW joint and BM are shown in Figure 10(a). According to the principle of metal electrochemical corrosion, there is the potential difference between dissimilar materials or different phases in the similar material. In the corrosive solution, electrons flow from low potential to high potential, and the material or phase with low potential will act as the anode to lose electrons and oxidation reaction occurs. In Al–Mg–Si series aluminum alloys, the potential of Si phase is higher than that of the Al matrix. Compared to that of the Al matrix, the potential of Mg_2Si phase in the alloy was lower [23]. Consequently, in 3.5% NaCl solution, the electrochemical reaction in the weldment is mainly caused by two kinds of galvanic couples, namely, Al–Mg_2Si and Al–Si. Because the potential of Mg_2Si phase is the lowest, the electrochemical reaction occurs first in the Al–Mg_2Si galvanic couple. The Mg_2Si phase with low potential is oxidized and the Al matrix as the cathode is protected.

The anode reaction is as follows:

$$Mg_2Si + 2H_2 \rightarrow 2Mg^{2+} + Si + 4H^+ + 8e^-. \quad (3)$$

The cathode reaction is as follows:

$$2H_2O + 2e^- \rightarrow H_2 + 2OH^-, \quad (4)$$

$$O_2 + 2H_2O + 4e^- \rightarrow 4OH^-. \quad (5)$$

The overall reaction equation in the electrochemical corrosion process of the Al–Mg_2Si galvanic couple is as follows:

Table 4: Electrochemical corrosion parameters of samples in 3.5% NaCl solution

Sample no.	self-corrosion current density (μA·cm^{-2})	self-corrosion potential (V)
BM	78.39	−0.650
AW	26.89	−0.578
HT1	33.14	−0.583
HT2	50.70	−0.592
HT3	72.41	−0.604

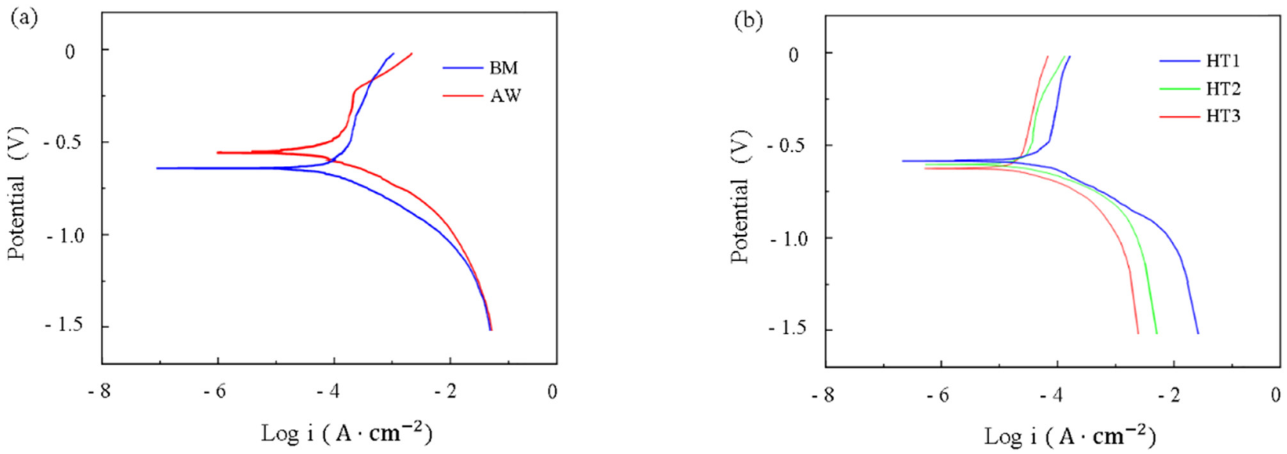

Figure 10: Tafel curves of different samples: (a) AW joint and BM and (b) PWHT joint.

$$Mg_2Si + O_2 + 2H_2O \rightarrow 2Mg(OH)_2 + Si. \quad (6)$$

With the continuous consumption of the Mg_2Si phase, the Si element is enriched, and the Al matrix with the low potential will act as working electrode to form Al–Si galvanic couple. At this time, the Al matrix is oxidized, and the anode reaction is as follows:

$$Al + 3OH^- \rightarrow Al(OH)_3 + 3e^-, \quad (7)$$

$$Al + 3Cl^- \rightarrow AlCl_3 + 3e^-. \quad (8)$$

The cathode reaction is the same as equation (4).

The overall reaction equation in the electrochemical corrosion process of Al–Si galvanic couple is as follows:

$$2Al + 3NaCl + 6H_2O \rightarrow 3H_2 + 3NaOH + Al(OH)_3 + AlCl_3. \quad (9)$$

With the occurrence of reaction equation (9), the reaction product is $Al(OH)_3$. As described in ref. [24], in the electrochemical reaction process, $Al(OH)_3$ could be converted into $Al_2O_3{\cdot}3H_2O$ to form the passivation film. Consequently, with the continuous proceeding of the reaction equation (9), the passivation ability of anode is enhanced, and the corrosion resistance is improved. From Table 4, the self-corrosion potential of the AW joint is −0.578 V, and that of the BM is −0.65 V. The self-corrosion potential of the AW joint is higher than that of the BM. The self-corrosion potential can intuitively reflect the corrosion resistance of the material. The higher the self-corrosion potential is, the better the corrosion resistance of material is.

The self-corrosion current density (I_{corr}) of the AW joint is 26.89 $\mu A{\cdot}cm^{-2}$, and that of the BM is 78.39 $\mu A{\cdot}cm^{-2}$. The self-corrosion current density of the AW joint is lower. The self-corrosion current density is positively correlated with the electrochemical corrosion rate, and the relationship between the two is described in formula (10) [25] as follows:

$$v_{corr} = \frac{3,270M \cdot I_{corr}}{\rho \cdot Z}, \quad (10)$$

where V_{corr} is the electrochemical corrosion rate ($mm{\cdot}year^{-1}$), M is the mass of the metal atom, I_{corr} is the self-corrosion current density ($A{\cdot}cm^{-2}$), ρ is the density of the material ($g{\cdot}cm^{-3}$), and Z is the number of the transferred electrons per metal atom. The lower self-corrosion current density indicates that the corrosion resistance of the AW joint is better than that of the BM. As shown in Figure 10(a), anode passivation occurs in the polarization curve of the AW joint. During EBW process, Mg element is probably lost by evaporation. Compared with that of the BM, the precipitation of Mg-containing β″ phase in the weldment is decreased, and the relative content of Si element is increased. As a result, the reaction equation (9) mainly occurs in the AW joint in the electrochemical corrosion process. The self-corrosion potential of the AW joint is higher, the self-corrosion current density is lower, and the anode passivation occurs. Consequently, the electrochemical corrosion resistance of the AW joint is better than that of the BM.

The Tafel curves of different PWHT joints are shown in Figure 10(b). From the self-corrosion potential and self-corrosion current density in Table 4, the electrochemical corrosion resistance of joints under different PWHT conditions is ranked as follows: HT1 > HT2 > HT3. With the increase in aging time, the corrosion resistance of joint presents the downward trend. After PWHT, the quantity of Mg_2Si phase in the weldment is increased, and the relative content of Si element is decreased. The difference in self-corrosion potential between the PWHT joint and the AW joint is not much high, while the anode passivation of the PWHT joint is not obvious. PWHT promotes the precipitation of β″ phase or β phase in the weldment, thus the reaction equation (6) easily occurs in the electrochemical corrosion process. The passivation of weldment becomes weaker. After PWHT, the electrochemical corrosion resistance of joint is decreased to a certain extent, which is related to the aging time. The longer the aging time is, the relatively large the precipitation of strengthening phase is, and the corrosion resistance is obviously decreased.

In the Al–Mg–Si series aluminum alloys and their welded joints, the potential of the Mg_2Si phase is lower than that of the Al matrix, thus it is first corroded and consumed in the Al–Mg–Si alloys. The schematic diagram of micro-galvanic corrosion process of both the Mg_2Si and Si phases in the aluminum alloy is shown in Figure 11. The Al–Mg_2Si micro-couple is corroded first, the Mg_2Si phase is the anode and the oxidation reaction occurs, and the Al matrix is the cathode. When the Mg_2Si phase acts as the anode, corrosion first occurs on the surface of Mg_2Si phase to form pitting corrosion, as shown in Figure 11(b). Because Mg element is relatively active, in the corrosion process, Mg element is consumed, which makes the Si element enriched in the Al matrix. The potential of the Si phase is relatively high compared with that of the Al matrix, and it acts as the cathode during the corrosion process. When the Mg element is consumed greatly, the polarity of Al matrix is converted from the original cathode to the anode. Subsequently, the Al–Si micro-couple begins to be corroded, as shown in Figure 11(c).

3.3.2 Intergranular corrosion behavior

Figure 12 shows the intergranular corrosion morphology of the AW joint, and the corrosion characteristic in the three regions of the joint is similar. Pitting corrosion appears in these regions, and grain boundary corrosion is induced near the corrosion pits. There exists intergranular corrosion tendency in weld zone. As shown in Figure 12(a)–(c), the maximum corrosion depth of the BM is 54.9 μm, the HAZ is 48.8 μm, and the FZ is 45.7 μm, respectively.

Figure 13 shows the intergranular corrosion morphology of the joint after PWHT. As shown in Figure 13(a), there is obvious reticular intergranular corrosion morphology in the HT1 joint, and exfoliation corrosion occurs on the sample surface, with the maximum corrosion depth of 240.9 μm. Compared with that of the AW joint, the corrosion resistance of the HT1 joint is significantly decreased. The corrosion morphology of the HT2 joint is mainly pitting corrosion, as shown in Figure 13(b). The maximum corrosion depth is 96.3 μm, and no obvious intergranular corrosion is generated, which is different from the corrosion morphology of the HT1 joint. As shown in Figure 13(c), severe reticular intergranular corrosion appears in the HT3 joint, and there is obvious exfoliation corrosion on the sample surface, with the maximum corrosion depth of 262.8 μm. In comparison, the corrosion resistance of the HT3 joint is the worst among the PWHT joints, and the surface exfoliation of sample is more serious.

The intergranular corrosion of Al–Mg–Si series aluminum alloys often develops from the pitting corrosion. If the intergranular corrosion is serious, it will further cause exfoliation corrosion. The corrosion degree of Al matrix is closely related to the content and distribution of Mg and Si elements. If the continuous corrosion channels are formed along the grain boundaries, the reticular intergranular corrosion will occur. When the element Mg/Si ratio in the Al–Mg–Si alloy is larger than 1.73, the relative content of Mg element is higher, and the tendency to pitting corrosion is increased. When the element Mg/Si ratio is lower than 1.73, the relative content of Si element

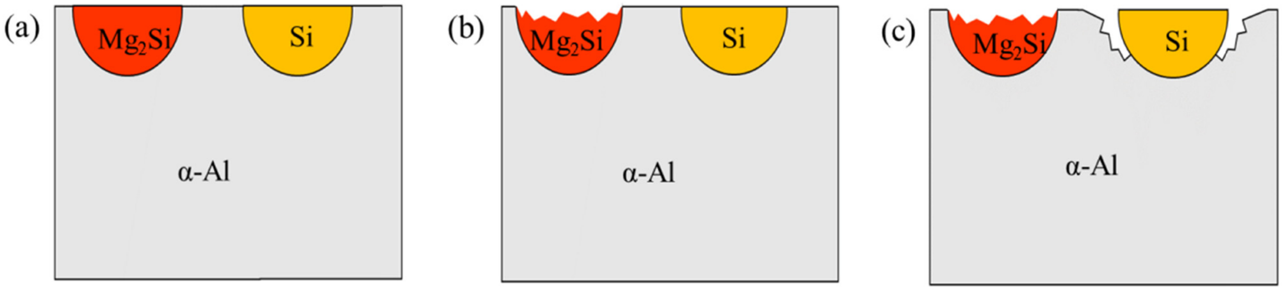

Figure 11: Schematic diagram of micro-galvanic corrosion process in Al–Mg–Si series aluminum alloys: (a) before corrosion, (b) Al–Mg_2Si galvanic corrosion, and (c) Al–Si galvanic corrosion.

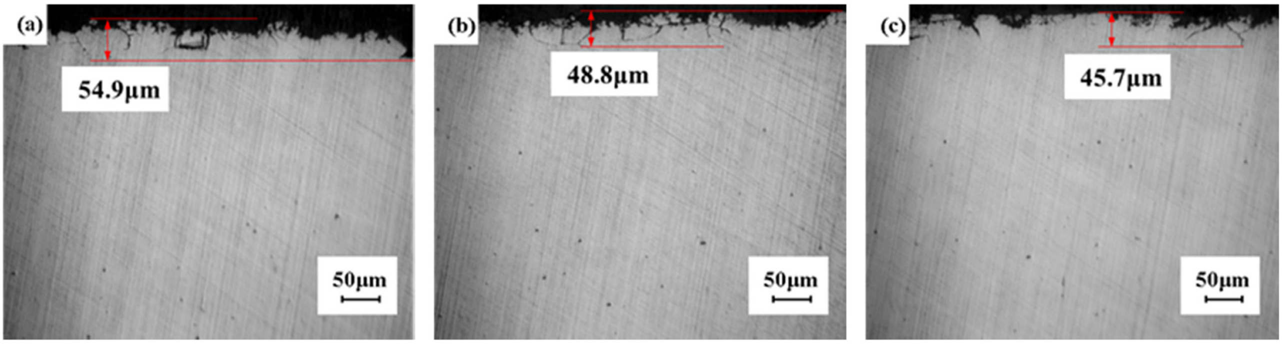

Figure 12: Intergranular corrosion morphologies of the AW joint: (a) BM, (b) HAZ, and (c) FZ.

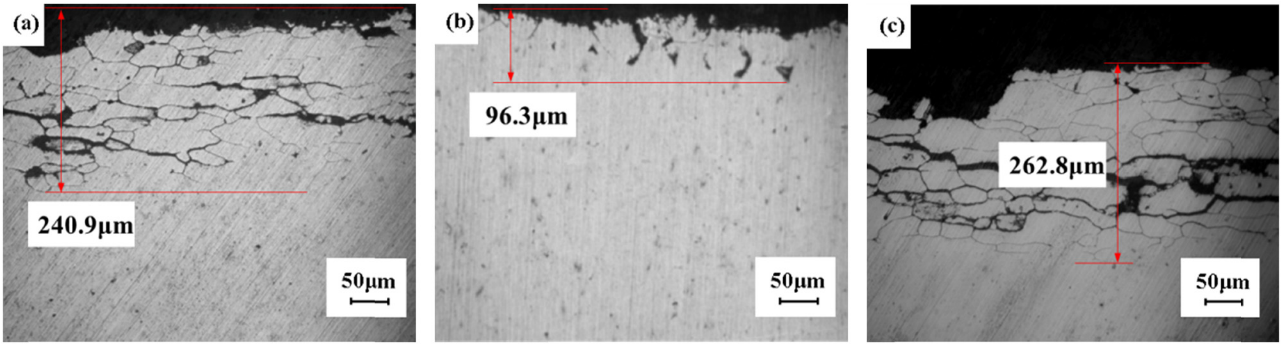

Figure 13: Intergranular corrosion morphology of the joint after PWHT: (a) HT1 joint, (b) HT2 joint, and (c) HT3 joint.

is higher, and the susceptibility to intergranular corrosion would be increased [26]. In the EBW process and subsequent heat treatment of aluminum alloy joint, the microstructure and distribution of alloying elements in the weldment are changed, which leads to the different corrosion resistance in different regions of the joint.

According to the intergranular corrosion morphology, the corrosion resistance of joint is closely related to the PWHT procedure. From the EDS analysis in Figure 5(b), the element Mg/Si ratio is 0.03 in the AW joint. Due to insufficient precipitation of the strengthening phases, the relative content of Si element is higher, and the quantity of precipitated phase in the weldment is obviously lower than that of the BM. The number of micro-couples is reduced, thus the corrosion resistance of the AW joint is better. The main corrosion type in the AW joint is pitting corrosion, and it also presents the tendency for intergranular corrosion. As shown in Figure 5(c) and (g), the quantity of precipitates in the HT1 and HT3 joints is significantly increased, and they tend to aggregate and distribute at grain boundaries, thus the continuous corrosion path is formed at grain boundaries. As a result, intergranular corrosion and exfoliation corrosion occur in the two joints.

The distribution of strengthening phases in the HT2 joint is relatively uniform, and no obvious aggregation occurs at grain boundary. According to the EDS analysis in Figure 5(f), the element Mg/Si ratio in the HT2 joint is 0.21, which is relatively large. Compared with that of the AW joint, the relative content of Si element in the HT2 joint is lower, which is advantageous to the corrosion resistance of joint. As shown in Figure 13, the corrosion morphology in the HT2 joint is mainly pitting corrosion and a little corrosion along the grain boundary. It has a certain tendency for intergranular corrosion, but no deep intergranular corrosion and exfoliation corrosion occur on the sample surface, which is dissimilar to the HT1 and HT3 joints. Among the three joints after PWHT, the HT2 joint has relatively good corrosion resistance.

In addition, the grain size in aluminum alloy had a certain effect on its corrosion resistance [27]. In the corrosive environment, the number of micro-couples formed inside the coarse grains is less than that of the fine grains. The corrosion resistance of coarse grain structure is better under the same condition. The HT2 joint has relatively good corrosion resistance. It is because the distribution of precipitates in the weldment is relatively uniform and no obvious aggregation at grain boundaries. Compared with that of the AW joint, the grain size of the HT2 joint is slightly increased. The number of micro-couples is relatively low, thus the corrosion resistance of the HT2 joint is better.

4 Conclusion

(1) The FZ is composed of columnar crystal and equiaxed grain in AW condition. There are mainly α-Al matrix phase, and some strengthening phases $\beta''(Mg_2Si)$ and $Q(Al_4CuMg_5Si_4)$ in the weld metal. After PWHT, a large amount of β'' phase and Q phase are precipitated in the weld zone, and the distribution of precipitated phases in the weldment is also improved, thus the mechanical property of joint is increased. The appropriate PWHT procedure is determined as follows: 550°C × 60 min + 175°C × 15 h.

(2) The hardness in FZ is obviously improved after PWHT, and the softening phenomenon is greatly decreased. In the HT2 condition, the tensile strength of welded joint reaches 273.9 MPa, which is 85.1% of that of the BM. There are many dimples on the fracture surface of joint, and it obviously presents the characteristic of ductile fracture.

(3) The resistance to electrochemical corrosion of the AW joint is relatively higher than that of the BM. The quantity of β'' phase precipitated in the weldment is lower in AW condition, and the anode passivation occurs during the electrochemical corrosion process. The more β'' phase or β phase is precipitated in the weldment after PWHT, the passivity of weldment is weakened. Consequently, the electrochemical corrosion performance of joint is decreased to a certain extent.

(4) In AW condition, the resistance to the intergranular corrosion of FZ is higher than that of the BM. Due to the insufficient precipitation of strengthening phases in the weldment, the number of micro-galvanic couples in the weldment is reduced compared with that of the BM. The resistance to the intergranular corrosion of the PWHT joints is lower than that of the AW joint. The distribution of strengthening phases in the weldment is relatively uniform after HT2 heat treatment, thus its intergranular corrosion resistance is the best among them.

Funding information: This project is supported by the Priority Academic Program Development of Jiangsu Higher Education Institutions (PAPD), which is gratefully acknowledged.

Author contributions: Shaogang Wang: methodology, supervision, and writing – review and editing; Junke Xu: investigation, formal analysis, and writing – original draft; Yongpeng Wang: resources, experimental preparation, and formal analysis.

Conflict of interest: The authors state no conflict of interest.

References

[1] Duan, C. F., S. L. Yang, J. X. Gu, Q. Xiong, and Y. Wang. Study on microstructure and fatigue damage mechanism of 6082 aluminum alloy T-type metal inert gas (MIG) welded joint. *Applied Sciences*, Vol. 8, No. 10, 2018, id. 1741.

[2] Lequeu, P., P. Lassince, and T. Warner. Aluminum alloy development: For the airbus A380-Part 2. *Advanced Materials and Processes*, Vol. 165, No. 7, 2007, pp. 41–44.

[3] Baghdadi, A. H., Z. Sajuri, M. Z. Omar, and A. Rajabi. Friction stir welding parameters: Impact of abnormal grain growth during post-weld heat treatment on mechanical properties of Al–Mg–Si welded joints. *Metals*, Vol. 10, No. 12, 2020, id. 1607.

[4] Baghdadi, A. H., Z. Sajuri, A. Keshtgar, N. M. Sharif, and A. Rajabi. Mechanical property improvement in dissimilar friction stir welded Al5083/Al6061 joints: Effects of post-weld heat treatment and abnormal grain growth. *Materials*, Vol. 15, No. 1, 2022, id. 288.

[5] Gu, J. X., S. L. Yang, C. F. Duan, Q. Xiong, and Y. Wang. Microstructure and mechanical characterization of laser welded 6013 aluminum alloys overlap joint. *Key Engineering Materials*, Vol. 795, 2019, pp. 49–53.

[6] Baghdadi, A. H., A. Rajabi, N. F. M. Selamat, Z. Sajuri, and M. Z. Omar. Effect of post-weld heat treatment on the mechanical behavior and dislocation density of friction stir welded Al6061. *Materials Science and Engineering A*, Vol. 754, 2019, pp. 728–734.

[7] Ahmad, R. and M. A. Bakar. Effect of a post-weld heat treatment on the mechanical and microstructure properties of AA6061 joints welded by the gas metal arc welding cold metal transfer method. *Materials and Design*, Vol. 32, No. 10, 2011, pp. 5120–5126.

[8] Wang, H., X. Liu, and L. Liu. Research on laser-TIG hybrid welding of 6061-T6 aluminum alloys joint and post heat treatment. *Metals*, Vol. 10, No. 1, 2020, id. 130.

[9] Viscusi, A., C. Leitão, D. M. Rodrigues, F. Scherillo, A. Squillace, and L. Carrino. Laser beam welded joints of dissimilar heat treatable aluminium alloys. *Journal of Materials Processing Technology*, Vol. 236, 2016, pp. 48–55.

[10] Sheng, X. F., K. Li, W. K. Wu, Y. Yang, Y. Liu, Y. F. Zhao, et al. Microstructure and mechanical properties of friction stir welded joint of an aluminum alloy sheet 6005A-T4. *Metals*, Vol. 9, No. 11, 2019, id. 1152.

[11] Svenningsen, G., J. E. Lein, A. Bjørgum, J. H. Nordlien, Y. Yu, and K. Nisancioglu. Effect of low copper content and heat treatment on intergranular corrosion of model AlMgSi alloys. *Corrosion Science*, Vol. 48, No. 1, 2006, pp. 226–242.

[12] Svenningsen, G., M. H. Larsen, J. H. Nordlien, and K. Nisancioglu. Effect of high temperature heat treatment on intergranular corrosion of AlMgSi(Cu) model alloy. *Corrosion Science*, Vol. 48, No. 1, 2006, pp. 258–272.

[13] Svenningsen, G., M. H. Larsen, J. H. Nordlien, and K. Nisancioglu. Effect of thermomechanical history on intergranular corrosion of extruded AlMgSi(Cu) model alloy. *Corrosion Science*, Vol. 48, No. 12, 2006, pp. 3969–3987.

[14] Kermanidis, A. T., A. D. Zervaki, V. Modas, A. N. Chamos, and S. G. Pantelakis. Fatigue performance of pre-corroded 6××× aluminum alloy laser beam welds with dissimilar heat treatment. *Procedia Engineering*, Vol. 74, 2014, pp. 22–26.

[15] Zhou, H. L., F. L. Fu, Z. X. Dai, Y. X. Qiao, J. Chen, and W. Liu. Effect of laser power on microstructure and micro-galvanic corrosion behavior of a 6061-T6 aluminum alloy welding joints. *Metals*, Vol. 11, No. 1, 2021, id. 3.

[16] Sun, X. G., X. X. Xu, Z. H. Wang, and Z. Y. Liu. Study on corrosion fatigue behavior and mechanism of 6005A aluminum alloy and welded joint. *Anti-Corrosion Methods and Materials*, Vol. 68, No. 4, 2021, pp. 302–309.

[17] Sravanthi, S. S., S. G. Acharyya, J. Joardar, and V. N. S. K. Chaitanya. A study on corrosion resistance and mechanical performance of 6061 aluminium alloy: galvanized mild steel electron beam welds at varying welding parameters. *Transactions of the Indian Institute of Metals*, Vol. 73, No. 4, 2020, pp. 881–895.

[18] Chakraborty, S., S. Sarkar, and P. Dutta. Effect of constitutional supercooling on the numerical solution of species concentration distribution in laser surface alloying. *Metallurgical and Materials Transactions B*, Vol. 32, No. 5, 2001, pp. 969–972.

[19] Miao, W. F. and D. E. Laughlin. A differential scanning calorimetry study of aluminum alloy 6111 with different pre-aging treatments. *Journal of Materials Science Letters*, Vol. 19, No. 3, 2000, pp. 201–203.

[20] Yin, Q. X., G. Q. Chen, X. Shu, B. G. Zhang, C. Li, Z. B. Dong, et al. Analysis of interaction between dislocation and interface of aluminum matrix/second phase from electronic behavior. *Journal of Materials Science and Technology*, Vol. 136, 2023, pp. 78–90.

[21] Zhang, W. K., H. He, C. C. Xu, W. Y. Yu, and L. X. Li. Precipitates dissolution, phase transformation, and re-precipitation-induced hardness variation in 6082-T6 alloy during MIG welding and subsequent baking. *The Journal of the Minerals, Metals and Materials Society*, Vol. 71, No. 8, 2019, pp. 2711–2720.

[22] Ravi, C. and C. Wolverton. First-principles study of crystal structure and stability of Al–Mg–Si-(Cu) precipitates. *Acta Materialia*, Vol. 52, No. 14, 2004, pp. 4213–4227.

[23] Birbilis, N. and R. G. Buchheit. Electrochemical characteristics of intermetallic phases in aluminium alloys: An experimental survey and discussion. *Journal of the Electrochemical Society*, Vol. 152, No. 4, 2005, pp. 140–151.

[24] Badawy, W. A., F. M. Al-Kharafi, and A. S. El-Azab. Electrochemical behaviour and corrosion inhibition of Al, Al-6061 and Al-Cu in neutral aqueous solutions. *Corrosion Science*, Vol. 41, No. 4, 1999, pp. 709–727.

[25] Deepa, P. and R. Padmalatha. Corrosion behaviour of 6063 aluminium alloy in acidic and in alkaline media. *Arabian Journal of Chemistry*, Vol. 10, No. S2, 2017, pp. 2234–2244.

[26] Zeng, F. L., Z. L. Wei, J. F. Li, C. X. Li, X. Tan, Z. Zhang, et al. Corrosion mechanism associated with Mg_2Si and Si particles in Al–Mg–Si alloys. *Transactions of Nonferrous Metals Society of China*, Vol. 21, No. 12, 2011, pp. 2559–2567.

[27] Qin, J., Z. Li, M. Y. Ma, D. Q. Yi, and B. Wang. Diversity of intergranular corrosion and stress corrosion cracking for 5083 Al alloy with different grain sizes. *Transactions of Nonferrous Metals Society of China*, Vol. 32, No. 3, 2022, pp. 765–777.